PHILOSOPHICAL TRANSACTIONS A

royalsocietypublishing.org/journal/rsta

Research

Cite this article: Kapancik Ülker E, Mohammadzadeh K, Hirani P, He Y, Guan S, Lahiri A. 2026 Mechanism of Zn storage in polyaniline in deep eutectic solvent–water mixtures: effect of anion and interfacial phenomena. *Phil. Trans. R. Soc. A* **384**: 20240474.
https://doi.org/10.1098/rsta.2024.0474

Received: 17 July 2025
Accepted: 10 September 2025

One contribution of 14 to a theme issue 'Surfaces, interfaces and heterogeneous catalysis'.

Subject Areas:
physical chemistry, chemical engineering, materials science

Keywords:
Zn-ion battery, spectroelectrochemistry, deep eutectic solvents, polyaniline, interface

Author for correspondence:
Abhishek Lahiri
e-mail: abhishek.lahiri@brunel.ac.uk

Electronic supplementary material is available online at https://doi.org/10.6084/m9.figshare.c.8369279.

THE ROYAL SOCIETY PUBLISHING

Mechanism of Zn storage in polyaniline in deep eutectic solvent–water mixtures: effect of anion and interfacial phenomena

Emine Kapancik Ülker[1], Kazem Mohammadzadeh[2], Pranay Hirani[2], Yinghe He[2], Shaoliang Guan[3] and Abhishek Lahiri[2]

[1]Recep Tayyip Erdogan University, Rize, Turkey
[2]Brunel University of London, London, UK
[3]University of Cambridge, Cambridge, UK

AL, 0000-0001-8264-9169

Zn-ion batteries (ZIBs) are promising energy storage devices, wherein both the electrode and electrolytes play a pivotal role. Aqueous electrolytes have a limited electrochemical window that reduces the energy density of the battery. In comparison, deep eutectic solvents (DES) have a wider electrochemical window that can offer a higher energy density. In this paper, the performance of Zn-ion batteries in formamide-based DES containing Zn salts of different anions (Cl^-, SO_4^{2-}, Ac^- and TfO^-) was investigated. The study revealed that anions significantly influence Zn solvation, hydrogen evolution reaction (HER), charge storage mechanism and stability of the battery. X-ray photoelectron spectroscopy (XPS), Raman spectroscopy and charge–discharge analyses showed that both chlorine and triflate anions store charge by anion exchange followed by Zn storage in polyaniline. For acetate and sulfate anions, the storage mechanism is by direct interaction of Zn with Zn-polyaniline (PANI). Among the four anions studied, the dual-storage mechanism in $ZnCl_2$- and ZnTfO-based DES electrolytes resulted in a more stable Zn–PANI battery performance. However, $ZnCl_2$-based DES electrolytes led to corrosive issues that affected the long-term stability. The

study provides useful insights on novel electrolyte development through manipulating the solvation chemistry of the molecules and the electrode/electrolyte interface.

This article is part of the theme issue 'Surfaces, interfaces and heterogeneous catalysis'.

1. Introduction

Zn-ion batteries (ZIBs) are gaining momentum as a cost-effective alternative to other metal-ion batteries [1,2]. The main advantages of ZIBs are the low cost, high theoretical capacity (820 mAh g^{-1}), safety of Zn metal, stability in aqueous electrolytes and ease of recyclability [3]. A typical ZIB consists of a Zn anode, an aqueous/non-aqueous electrolyte, a separator and a suitable cathode (metal oxides, carbon-based material, polymers, etc.). However, challenges related to storage of Zn in the cathode, formation of Zn dendrite during cycling, low coulombic efficiency and dissolution of cathodes in the electrolyte leading to capacity fading still exist that makes the energy storage system far from being commercialized.

As electrolytes play a critical role in ZIBs, which define not only the electrochemical window but also the intercalation/deintercalation processes and deposition/stripping processes, it is important to tune the electrolyte to obtain high energy density and stability in ZIBs. Aqueous electrolytes have been extensively studied in ZIBs [4–7]. However, they have a limited electrochemical window, which is restricted by the electrocatalytic hydrogen evolution reaction (HER). Various cathode materials such as metal oxides, conducting polymers and carbon-based materials have been studied in aqueous electrolytes in ZIBs [8–10]. Issues related to Zn dendrite formation, cathode dissolution and HER were identified. Parasitic side reactions significantly hinder the performance of ZIBs. HER reduces coulombic efficiency by consuming electrons and electrolyte through water decomposition ($Zn + 2H_2O \rightarrow Zn(OH)_2 + H_2$) [11,12]. In addition, it contributes to the formation of zinc hydroxide precipitates, which accelerate surface passivation, promote dendritic zinc growth and lead to local pH fluctuations. These processes not only degrade the structural stability of the zinc anode through corrosion and passivation but also result in irreversible loss of active materials [13–15]. To address these challenges, electrolyte modification has emerged as a promising strategy. Modification of the electrolyte was shown to be a useful technique to obtain better stability [16]. For example, 1M zinc triflate ($Zn(CF_3SO_3)_2$) concentration showed lower columbic efficiency for Zn deposition/stripping compared to 3M $Zn(CF_3SO_3)_2$, which is due to the change in the solvation of Zn ions in the electrolyte [17]. However, its influence on the cathode chemistry was not studied in detail.

Besides aqueous electrolytes, non-aqueous electrolytes such as ionic liquids and deep eutectic solvents (DES) have recently been researched in ZIBs [18–21]. Although both ionic liquids and DES improve the electrochemical window, thereby increasing the energy density, issues related to high viscosity and lower ionic conductivity hamper the performance of ZIBs. Therefore, more recent research towards ionic liquid–water electrolytes and DES–water electrolytes is being investigated as alternatives for ZIB. The presence of ionic liquids/DES in aqueous electrolytes changes the Zn solvation in the bulk of the electrolyte, which then changes the electrode/electrolyte interface and improves the Zn deposition/stripping at the anode [22–24]. For example, Lu *et al*. showed that a low-concentration eutectic electrolyte made by adding *N*-methyl-2-pyrrolidone (NMP) to an aqueous solution of 2M Zn triflate led to the formation of $[Zn(H_2O)_4NMP]^{2+}$ ion complexes. The complex helped improve the ZIB performance compared to the aqueous electrolyte [25]. Similarly, water in DES has been shown to enable better Zn deposition/stripping at higher current densities. It was shown that the addition of 30 mol% H_2O in a eutectic mixture of urea, lithium bis(trifluoromethanesulfonyl)imide and zinc bis(trifluoromethanesulfonyl)imide led to the formation of a complex network of water molecules in the electrolyte with the establishment of hydrogen bonding and a coordinating network. This complexation led to the suppression of the reactivity of the Zn anode and

thereby improved the Zn deposition/stripping cycles [26]. In the case of ionic liquid/DES–water electrolytes, most studies have concentrated on the Zn deposition/stripping, and little has been investigated on its effect on the cathode.

In this paper, we describe a detailed study of the effect of an anion in a DES–water electrolyte for ZIBs. The DES was a mixture of formamide (high dielectric constant of 109) and various Zn salts in a 1 : 4 ratio with 40% water added to the electrolyte. The electrolyte composition was chosen based on our recent study, which showed that when the water concentration in the DES was below 30%, a porous Zn morphology was obtained, whereas above this, a thick crystalline Zn deposit was obtained [27]. Both electrochemical and spectroscopic studies were conducted for a Zn-polyaniline (PANI) system, and the Zn storage mechanism in PANI was investigated using X-ray photoelectron spectroscopy (XPS) and *in situ* Raman spectroelectrochemistry. The results suggest that anion plays a significant role in altering the electrochemistry and charge storage mechanism of Zn at the polymer cathode.

2. Experimental

Zn acetate (99.99%), Zn sulfate (98%), Zn chloride (99%), Zn triflate (98%) and Aniline (98%) were purchased from Fisher Scientific; Zn (99.9%) was purchased from Pi-Kem and graphite paper from RS Pro. The electrolytes were prepared by mixing various zinc salts in formamide at 70°C for 2 h. The solution was subsequently cooled to room temperature, after which water was added to the electrolyte and the mixture was stirred at room temperature for 24 h.

Polyaniline was electrochemically deposited on to the graphite paper from 0.1M H_2SO_4 solution containing 0.1M aniline. The deposition was performed by first electrochemically depositing at 1 mA cm^{-2} current for 5 min followed by cycling between a potential of −0.5 and 1.2 V versus Ag/AgCl. Six cyclic voltammetry (CV) cycles were performed to obtain polyaniline on the carbon paper. The deposit was then washed in water and dried in a vacuum oven at 60°C for 2 h. The mass loading was found to be approximately 1 mg cm^{-2}. Electronic supplementary material, fig. S1, shows the optical and microstructure of PANI.

The corrosion and hydrogen evolution behaviour of the Zn electrode in different electrolytes was investigated using an electrochemical cell with a Zn plate as the working electrode, a carbon plate as the counter electrode and Ag/AgCl as the reference electrode. The Tafel corrosion measurements were conducted within a potential range of −0.7 to 1.2 V (versus Ag/AgCl) at a scan rate of 5 mV s^{-1}. The performance of HER was evaluated by linear sweep voltammetry in the potential range of −0.9 to 1.1 V versus Ag/AgCl at a scan rate of 5 mV s^{-1}.

Electrochemical measurements were carried out in a split cell consisting of a polyaniline-coated graphite electrode as the working electrode, Zn foil as the counter and reference electrodes with different electrolytes. The CV was performed in the potential range of 0–1.8 V vs Zn at different scan rates from 0.1 to 1 mV s^{-1} by using a Biologic VMP 3e potentiostat/galvanostat. The galvanostatic charge/discharge cycling tests were carried out in a split cell with a Zn anode, a Whatman separator, and a polyaniline cathode with different electrolytes, by using a battery tester, Nanocycler from Nanobase.

XPS analysis was performed using a Thermo NEXSA XPS fitted with a monochromated Al kα X-ray source (1486.7 eV), a spherical sector analyser and three multichannel resistive plate, 128 channel delay line detectors. All data were recorded at 19.2 W and an X-ray beam size of 400 × 200 µm. Survey scans were recorded at a pass energy of 200 eV, and high-resolution scans were recorded at a pass energy of 40 eV. Electronic charge neutralization was achieved using a dual-beam low-energy electron/ion source (Thermo Scientific FG-03). The ion gun current was 150 µA, and the ion gun voltage was 45 V. All sample data were recorded at a pressure below 10^{-8} Torr and a room temperature of 294 K. Data were analysed using CasaXPS v. 2.3.20PR1.0.

Infrared (IR) and Raman spectra of the electrolyte and the polymer were acquired using Shimadzu IRspirit and Renishaw inVia confocal Raman microscope, respectively. For the *in situ* Raman spectroelectrochemical study, the electrochemical cell from Redox.me was used and

placed under the Raman microscope. The Raman microscope is equipped with a 514 nm laser (Stellar-REN) and uses a diffraction grating of 1800 lines mm^{-1} with a Renishaw CCD camera as the detector. The electrochemical cell with the PANI exposed to the Raman laser and Zn as counter and reference electrode was connected to Biologic SP-50 potentiostat/galvanostat, and charge–discharge studies were conducted within the electrochemical cell. For the Raman tests, the samples were run with laser power at 100% using the 5× objective lens with a 532 nm laser.

3. Results and discussion

The zinc solvation in the electrolyte was first investigated using Fourier transform IR (FTIR) and Raman spectroscopy. Figure 1 compares the IR and Raman spectra of the different electrolytes. From the IR spectra in figure 1a, it is evident that, based on the Zn salts, changes occur in the symmetric bending mode of NH_2 in the formamide [28]. In the case of chloride and acetate anions, the symmetry of the peak changes, whereas for the case of sulfate and triflate anions, the peak forms a shoulder. The changes in this peak suggest that intermolecular forces and the interaction with formamide are stronger in sulfate and triflate salts. This is further confirmed by the significant loss/change in the CN stretching at 1315 cm^{-1}. For the case of sulfate and triflate Zn salts, additional vibrational peaks of S–O and CF_3 are observed in the IR spectra (figure 1a).

The Raman spectra of the electrolytes are shown in figure 1b from which it is evident that different Zn salt-containing electrolytes show different vibration modes. The changes in the CN peaks shown in the IR spectra can also be seen in the Raman spectra in figure 1c. It is evident that the CN peak shifts depend on the Zn salt as well as the area of the peak changes, which indicates an interaction between the Zn salt and formamide. Although it is possible to quantify the Zn coordination number from fitting the CN vibration in the Raman spectra, as shown previously [28], a large presence of water leads to a quantification error that indicates that the Zn salt interacts with both formamide and water [27].

We then studied the electrolyte interaction with Zn to understand the corrosion and HER properties of the different electrolytes. Figure 2a presents the corresponding Tafel plots, from which the corrosion potentials (E_{corr}) were determined by extrapolating the linear regions of the curves. Accordingly, the E_{corr} values are −0.955, −0.984, −1.023 and −0.905 V for $ZnCl_2$, $ZnSO_4$, ZnAc and ZnTfO, respectively, indicating that ZnAc inhibits the corrosion of the Zn electrode. Among these electrolytes, ZnAc also exhibits the most negative overpotential for HER (figure 2b), suggesting suppressed HER activity. To reach a current density of 5 mA cm^{-1}, potentials of −1.18, −1.095 and −1.047 V were required in $ZnSO_4$, $ZnCl_2$ and ZnTfO electrolytes, respectively (figure 2b). These findings show that ZnAc and $ZnSO_4$ more effectively restrict the side reaction compared to $ZnCl_2$ and ZnTfO, which is consistent with the corrosion results [29]. Overall, Tafel and linear sweep voltammetry measurements demonstrate that the corrosion and HER behaviour of the Zn electrode are significantly influenced by the type of Zn salt present in the DES electrolytes.

Next, we studied the influence of the electrolytes on the PANI cathode. Figure 3 compares the CV of different DES electrolytes in the Zn–PANI system, from which it is evident that the anion of the Zn salt in the DES significantly affects the Zn electrochemistry. On using $ZnCl_2$ in the DES, the CV shows two reduction peaks at 1.02 and 0.9 V, which shift with scan rate. In the anodic scan, two oxidation waves at around 1 and 1.3 V are observed that shift with an increase in the scan rate. The oxidation peaks correspond to the reduction process that takes place in the cathodic scan. The association of pseudocapacitive behaviour with the surface reaction can be evaluated using equations (3.1) and (3.2) [30,31].

$$i = \log a + b \log \upsilon, \tag{3.1}$$

$$i = k_1 + k_2 \upsilon^{1/2}. \tag{3.2}$$

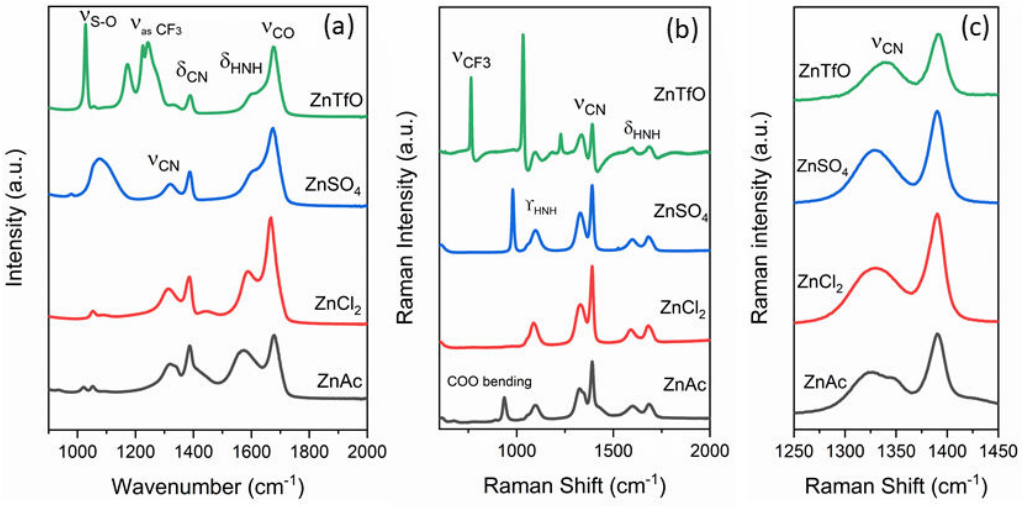

Figure 1. FTIR and Raman spectra of different electrolytes: (a) IR spectra, (b) Raman spectra and (c) magnified CN peak on the Raman spectra.

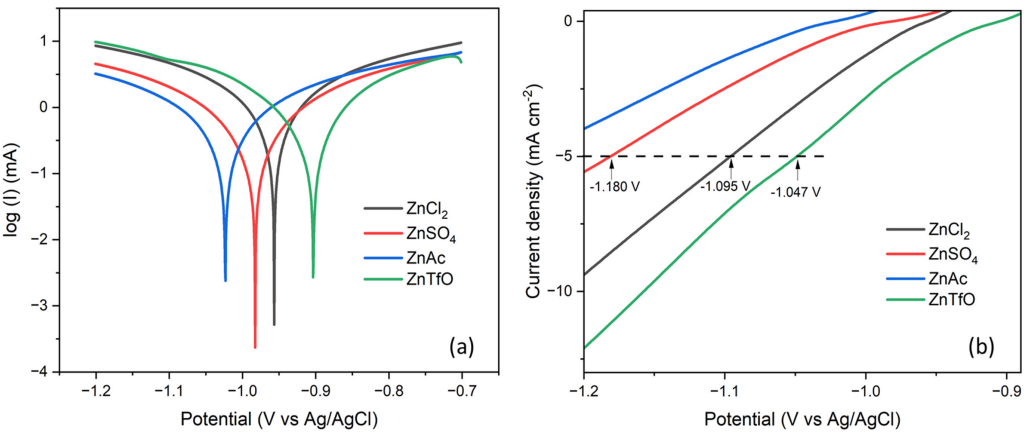

Figure 2. Comparison of Tafel plots (a) and HER performance (b) of Zn electrode in $ZnCl_2$, $ZnSO_4$, ZnAc and ZnTfO: formamide + 40 wt% water.

Using equation (3.1), the first oxidation peak at approximately 1.02 V corresponds to a capacitive process, as the plot of log of scan rate against log of peak current results in a *b*-value close to 1 (see electronic supplementary material, fig. S2a). The capacitive process can be related to the doping/dedoping of Cl on PANI [32]. The second oxidation peak at approximately 1.3 V corresponds to the interaction of Zn ions with PANI (figure 3a). On using equation (3.1), a '*b*'-value of 0.68 (electronic supplementary material, fig. S2b) is obtained, which relates to both capacitive and faradaic processes. Using equation (3.2), the contribution of both capacitive and faradaic processes is shown in electronic supplementary material, fig. S2c. Interestingly, the capacitive values calculated are low compared to aqueous electrolytes for the Zn–PANI battery and do not change significantly with scan rate [33,34]. This can be ascribed to the interaction between $ZnCl_2$, formamide and water that affects the doping/dedoping process. On changing the anion from $ZnCl_2$ to $ZnSO_4$, a significant change in the CV occurs (figure 3b). At a scan rate above 0.2 mV s^{-1}, a single oxidation and reduction peak is seen at approximately 1.3 and 1 V, respectively. Both these peaks shift with an increase in scan rate, which could be caused by a change in the surface processes on PANI. This change in the surface processes was supported

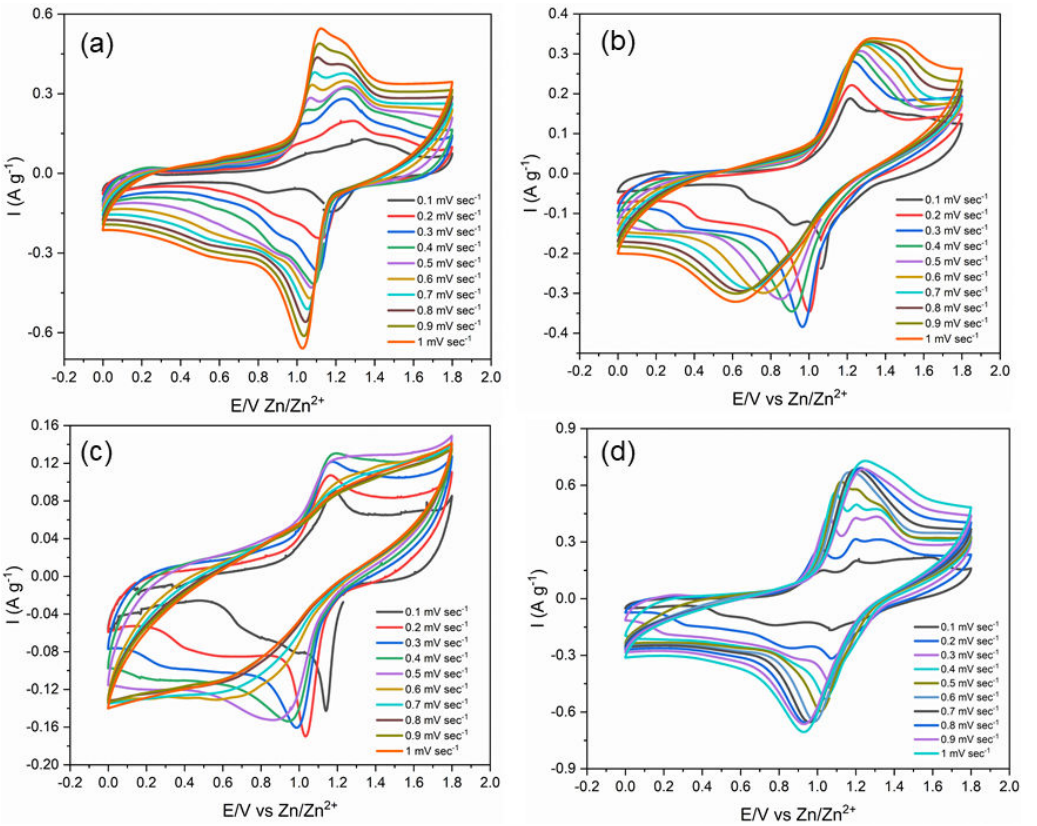

Figure 3. CV at different scan rates of PANI in the following electrolytes: (a) $ZnCl_2$: formamide + 40 wt% water, (b) $ZnSO_4$: formamide + 40 wt% water, (c) ZnAc: formamide + 40 wt% water and (d) ZnTfO: formamide + 40 wt% water.

by the fact that there was no linear shift with the scan rate or the square root of the scan rate. The oxidation/reduction process could therefore be ascribed to the interaction of Zn with PANI.

A similar observation in the CV curve was seen when using Zn acetate salt. An oxidation/reduction process is seen at approximately 1.2 and 1.1 V, which can be related to Zn interaction with PANI (figure 3c). At higher scan rates, the CV changes to almost a capacitive behaviour, suggesting a change in PANI surface. On changing the anion to triflate, two oxidation and two reduction peaks are observed at low scan rates (0.1–0.5 mV s^{-1}) at 1.0 and 1.2 V, and 1.05 and 0.8 V, respectively, which shift with scan rates. At higher scan rates, these peaks shift with potential and merge into a single oxidation/reduction peak at 1.3 and 0.9 V, respectively (figure 3d). On using equation (3.1), the *b*-value of 0.7 was obtained for the first oxidation peak, and a value of 0.68/0.8 was obtained for the second oxidation and reduction peak (electronic supplementary material, fig. S3a,b). This suggests that both capacitive and faradaic processes take place in the presence of ZnTfO, and the capacitive process owing to doping/dedoping cannot be distinguished as clearly as in the case of $ZnCl_2$. Again, the capacitive process was found to vary between 20 and 40% (electronic supplementary material, fig. S3c), which is different from aqueous electrolytes and can be related to the interaction forces in the DES as seen from the IR and Raman study. Based on the CV studies, it is clear that anions in DES significantly affect the adsorption/desorption and Zn electrochemistry on PANI, and the electrolyte interactions are different compared with those studied on the Zn anode.

Charge–discharge experiments were conducted to evaluate the performance of ZIB. Figure 4 compares the charge–discharge profiles at different current densities from 0.25 to 2 A g^{-1}. It is evident from figure 4 that the Zn-polymer battery shows the highest capacity on using $ZnCl_2$: formamide + 40 wt% water electrolyte (figure 4a) at every current density from 0.25 to 2 A

g^{-1}, showing a capacity of approximately 250 mAh g^{-1} at 0.25 A g^{-1}. The electrolytes containing $ZnSO_4$, ZnAc and ZnTfO all show similar capacity of approximately 110 mAh g^{-1} at 0.25 A g^{-1} (figure 4b–d).

The capacity loss is much higher on increasing the current density for $ZnSO_4$ and ZnAc–DES electrolyte compared to ZnTfO–DES-based electrolyte. It is evident from figure 4b–d that, at a current density above 1 A g^{-1}, the capacity of the Zn-polymer battery using $ZnSO_4$ and ZnAc–DES electrolytes decreases to below 50 mAh g^{-1}, whereas the ZnTfO–DES electrolyte-based battery shows a capacity greater than 55 mAh g^{-1}. This indicates that the presence of an anion in DES changes the PANI surface during charge–discharge that affects the Zn storage capability.

To understand the role of anions on the charge storage in the polymer, *ex situ* XPS of PANI was performed at different potentials in different DES electrolytes. The survey spectra at different potentials are shown in electronic supplementary material, fig. S4, from which peaks of C1s, N1s, O1s and Zn2p can clearly be identified. As the electrolyte interaction with the polymer would result in prominent changes in N1s, the high-resolution spectra of the N1s peak in figure 5 are examined in detail. The XPS spectra can be deconvoluted into various peaks. At open circuit potential (figure 5a), PANI shows peaks at 399.7, 402.1 and 403.3 eV. These peaks correspond to amine (–NH–), protonated imine (=NH^+) and (N–O), respectively [35–37]. During discharge in $ZnCl_2$–DES electrolytes (figure 5a), shifts in the peaks are observed. The N–O peak disappears on discharge, and a peak shift from protonated imine to protonated amine (–NH^+) at 401.1 eV is observed. The changes in the various N1 contributions for $ZnCl_2$-based DES are shown in figure 6a.

On further discharge, the peaks related to amine increase with a decrease in peaks of protonated imine and protonated amine (figure 6a). On charging the battery, a reverse phenomenon occurs where a decrease in amine and an increase in protonated amine and imine are observed. However, the N–O bond disappears, which suggests that no oxidation of PANI occurs. In comparison, on using $ZnSO_4$-based DES, a similar change is observed in the XPS spectra (figures 5b and 6b). On discharge, the disappearance of the N–O peak occurs with the occurrence of the protonated amine peak, which, on further discharge, decreases (figure 6b). At complete discharge, a non-protonated imine is observed with a contribution from amine. On charging, a change from non-protonated imine to amine takes place initially along with the formation of N–O (figures 5b and 6b). This further changes to an increase in protonated imine and N–O on further charging. On using ZnAc-based DES, a similar phenomenon is again noted (figures 5c and 6c). On discharge, protonated amine appears with an increase in amine peak, and during charge, the amine peak decreases with an increase in protonated amine and imine. In the case of ZnTfO-based DES, a slight change in the mechanism is observed during discharge, wherein a change from protonated amine to non-protonated amine is observed, which on charge changes to amine and protonated amine and imine (figures 5d and 6d).

Based on the XPS spectra, the electrodeposited PANI consists of both protonated and non-protonated nitrogen groups. During discharge, a reduction process occurs, which leads to the reduction of protonated nitrogen groups to non-protonated amine (–NH–). From figure 6, it can be seen that the extent of reduction changes with a change in the anion of the DES. The extent of reduction (increase in –NH–) is highest for $ZnCl_2$-based DES, which might have led to a higher specific capacity. In comparison, for the case of $ZnSO_4$ and ZnTfO, further reduction appears to have taken place to form imine. Furthermore, the protonated imine does not show an initial change in the peak for ZnAc-based electrolyte, indicating a change in the charge storage mechanism. It has been shown that during the doping/dedoping process for PANI, an increase in protonated amine and imine occurs [38]. This indicates that for ZnAc-based electrolyte, acetate doping does not occur, which is evident from the CV in figure 3c, and this leads to a change in PANI structure during Zn storage and causes a change in the CV behaviour seen in figure 3c. During charging, all except $ZnSO_4$-based DES electrolyte show the formation of protonated nitrogen groups, whereas N–O formation is observed for $ZnSO_4$-based

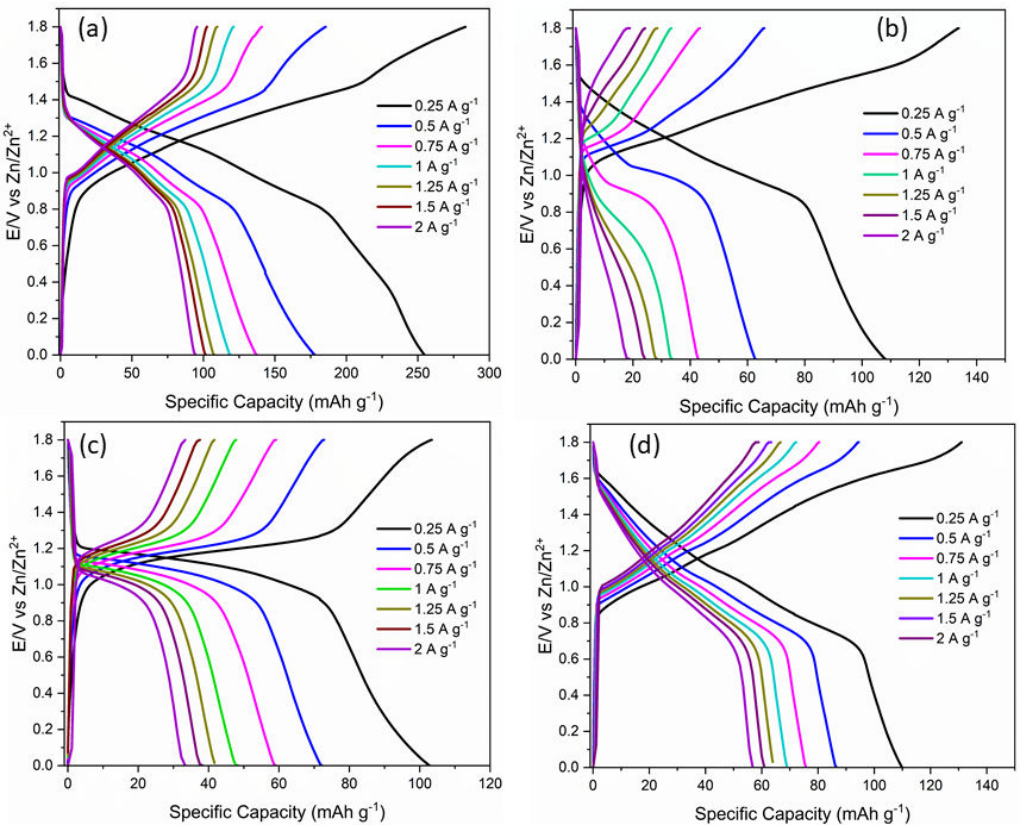

Figure 4. Charge–discharge profile of Zn–PANI at different current densities in the following electrolytes: (a) $ZnCl_2$: formamide + 40 wt% water, (b) $ZnSO_4$: formamide + 40 wt% water, (c) ZnAc: formamide + 40 wt% water and (d) ZnTf0: formamide + 40 wt% water.

DES electrolyte, which suggests a surface modification of PANI. This might be the cause for the change in the CV observed in figure 3b.

In situ Raman spectroscopy was further used to probe into the storage mechanism. Figure 7 shows the *in situ* Raman measurement of PANI in different electrolytes. Owing to the overlapping of the Raman spectra of the electrolyte with PANI, the peak related to C=C in the polyaniline structure at 1590 cm^{-1} was used to understand the changes during the charge–discharge process [39,40]. The full Raman spectra are shown in electronic supplementary material, fig. S5.

Examining the Raman spectra of PANI in $ZnCl_2$-based DES (figure 7a), it is evident that during the discharge process, peak broadening and a shift to higher wavenumbers occurred for C=C peak. The shift from open circuit potential to a fully discharged state (0D, figure 7a) was 5 cm^{-1}. The peak broadening can be related to doping of PANI owing to a change in anion that leads to differently ordered and charged PANI chains [41]. The shift to higher frequency occurs owing to deprotonation of PANI and Zn storage [39], which was also observed from the XPS measurements in figure 5. Consequently, on charging to 1.74 V, peak shrinking occurs along with a negative shift in the Raman spectra back to its original form, which indicates that protonation of PANI occurred. A similar phenomenon was recently observed during Al storage in PANI from an aqueous electrolyte [42]. For $ZnSO_4$-based electrolyte (figure 7b), during discharge, a shift of C=C band to higher wavenumbers is obvious. The shift is more significant compared to $ZnCl_2$-based DES; even at a lower discharge potential and at a fully discharged state, a shift of 10 cm^{-1} occurred. This rapid shift suggests that the deprotonation process of the PANI takes place early and leads to the formation of imine. On charging, a reverse of the

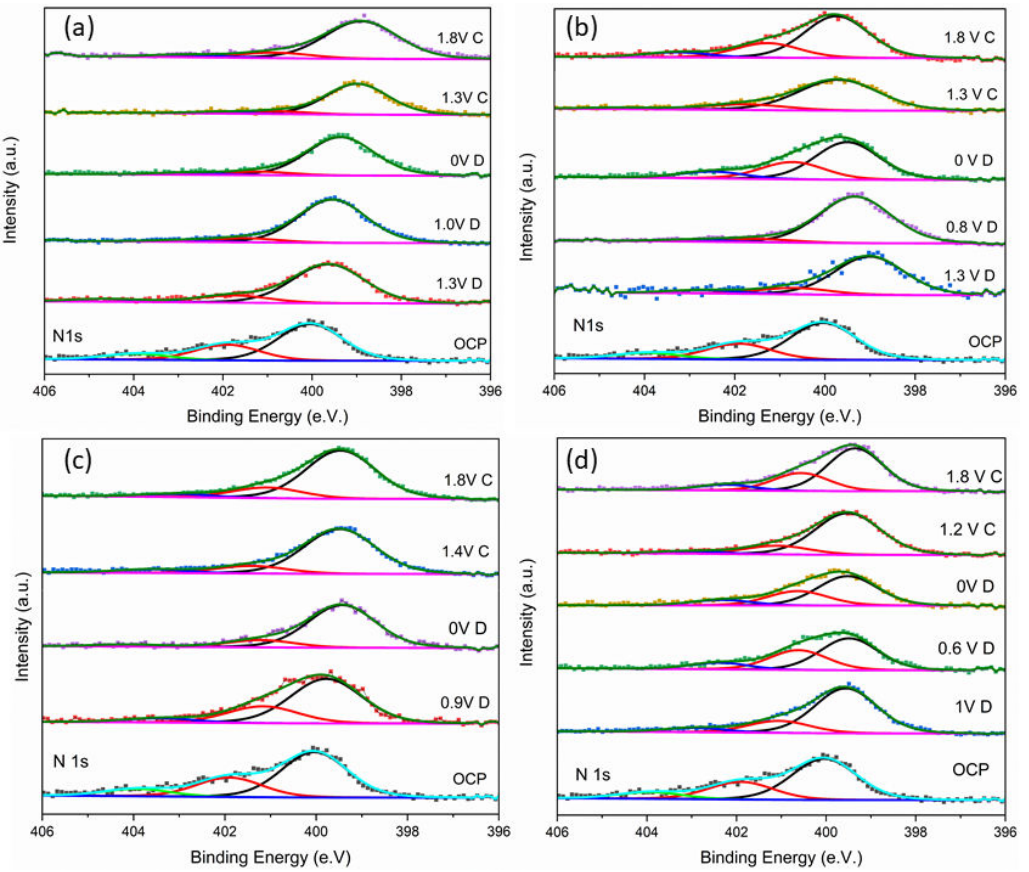

Figure 5. XPS of N1s spectra of PANI at different charge–discharge potentials in the following electrolytes: (a) $ZnCl_2$: formamide + 40 wt% water, (b) $ZnSO_4$: formamide + 40 wt% water, (c) ZnAc: formamide + 40 wt% water and (d) ZnTfO: formamide + 40 wt% water.

phenomena is observed. However, at 1.6 and 1.87 V, the C=C feature changed from the original structure, suggesting a slight change in the PANI structure, which was also observed in XPS measurements. On using ZnAc-based DES, the changes are insignificant (figure 7c), and a shift to higher wavenumbers during charging occurs by 3 cm^{-1} with insignificant peak broadening, which reverses to its original wavenumber when charged to 1.9 V. This is in good agreement with XPS results. In the case of ZnTfO-based DES (figure 7d), a peak broadening along with peak shift (7 cm^{-1}) to higher wavenumbers occurs during the discharge process and is reversed during charging. The peak shift during discharge is slightly lower compared to that observed for $ZnSO_4$ electrolyte, which again suggests that deprotonation to the imide structure might have taken place. However, during the charge to 1.7 V potential, a peak close to the original peak of PANI is observed and is in good agreement with the XPS results. Based on the Raman results, it appears that peak broadening is related to anion exchange, which can be associated with a capacitive process, whereas peak shifts indicate a faradaic process.

Based on the XPS, Raman and electrochemical analyses, the charge storage mechanism, as shown in scheme 1, is proposed. Initially, the electrodeposited PANI is in the charged state with sulfate anion, as it was electrodeposited in sulfuric acid electrolyte. For the case of $ZnCl_2$- and ZnTfO-based DES, a capacitive process first takes place owing to anion exchange, which is then followed by Zn storage in PANI. For ZnAc and $ZnSO_4$, no anion exchange occurs, and Zn is stored directly in the polymer matrix.

Finally, the cyclability of PANI in the Zn–PANI battery was tested to evaluate the stability in different electrolytes at a current density of 0.5 A g^{-1}. Figure 8 shows the charge–discharge

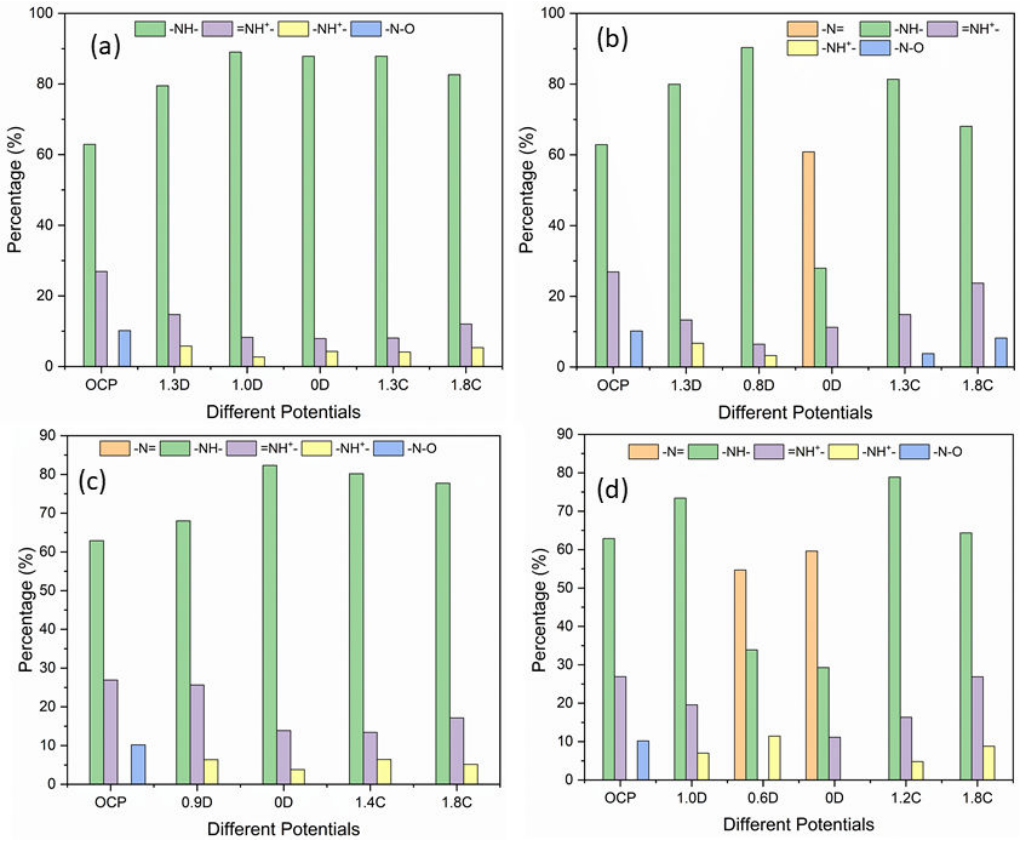

Figure 6. Calculated N content in PANI from the various peaks of N1s spectra in figure 5 at different charge–discharge potentials in the following electrolytes: (a) $ZnCl_2$: formamide + 40 wt% water, (b) $ZnSO_4$: formamide + 40 wt% water, (c) ZnAc: formamide + 40 wt% water and (d) ZnTfO: formamide + 40 wt% water.

cycles using different DES–water electrolytes. In $ZnCl_2$-based DES electrolyte, an initial capacity of about 200 mAh g^{-1} is obtained, which decreases to 130 mAh g^{-1} after 75 cycles. However, repeated experiments showed stability issues occurred beyond 70–75 cycles, which might be associated with the corrosive nature of the electrolyte on the Zn surface. In the case of $ZnSO_4$-based DES, a rapid decrease in capacity from 96 to 53 mAh g^{-1} is observed within the first 50 cycles, after which it nearly plateaus. A similar behaviour is seen for ZnAc-based DES electrolyte, wherein an initial capacity of 140 mAh g^{-1} is obtained and decreases to 48 mAh g^{-1} after 75 cycles. In comparison, for ZnTfO-based DES, a gradual decrease from 95 to 62 mAh g^{-1} is observed after 75 cycles.

Comparing the capacity loss, it is evident that for $ZnSO_4$- and ZnAc-based DES, the loss is faster and more (<53% capacity retention after 75 cycles) compared to $ZnCl_2$- and ZnTfO-based DES (65% capacity retention after 75 cycles). This is due to the difference in Zn storage mechanism as illustrated in Scheme 1, wherein a single-step Zn storage mechanism takes place for $ZnSO_4$- and ZnAc-based DES, whereas a two-step mechanism is observed for $ZnCl_2$- and ZnTfO-based DES. To understand the capacity loss, SEM and XPS of PANI were performed. Compared with the SEM of original deposited PANI in electronic supplementary material, fig. S6a, Zn deposits on PANI from $ZnSO_4$-based DES can be observed in electronic supplementary material, fig. S6c, which suggests that during Zn storage in PANI, some Zn deposition also takes place. The PANI morphology shows little change in the other three electrolytes (electronic supplementary material, fig. S6b,d–e). The XPS spectra after cycling in different electrolytes are compared in electronic supplementary material, fig. S7. It is evident from the survey spectra (electronic supplementary material, fig. S7a) that Zn remains trapped in the polymer matrix

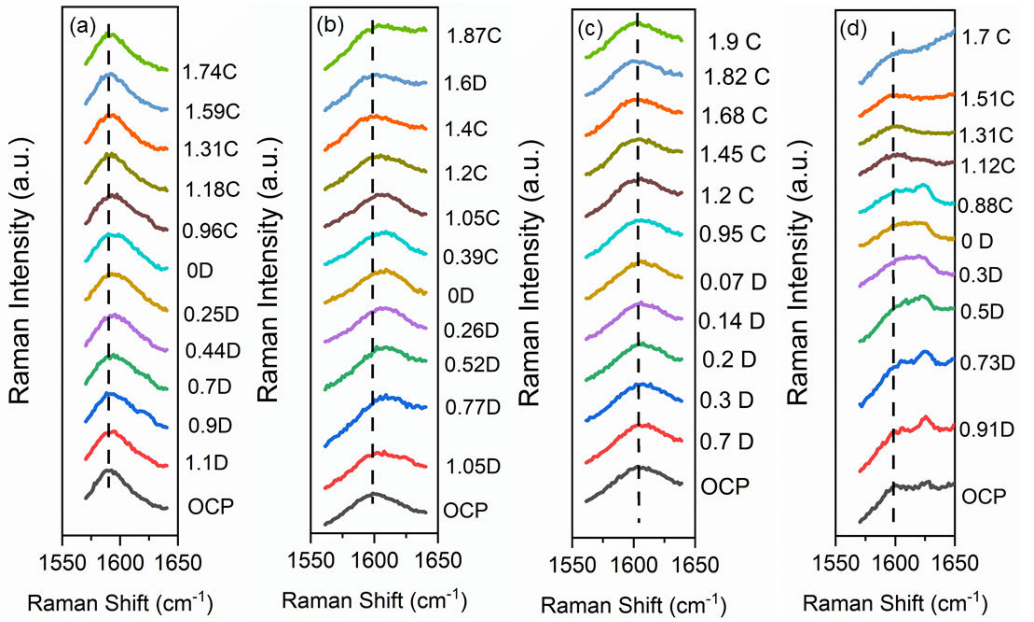

Figure 7. *In situ* Raman spectroelectrochemistry of PANI in the following electrolytes: (a) $ZnCl_2$: formamide + 40 wt% water, (b) $ZnSO_4$: formamide + 40 wt% water, (c) ZnAc: formamide + 40 wt% water and (d) ZnTfO: formamide + 40 wt% water.

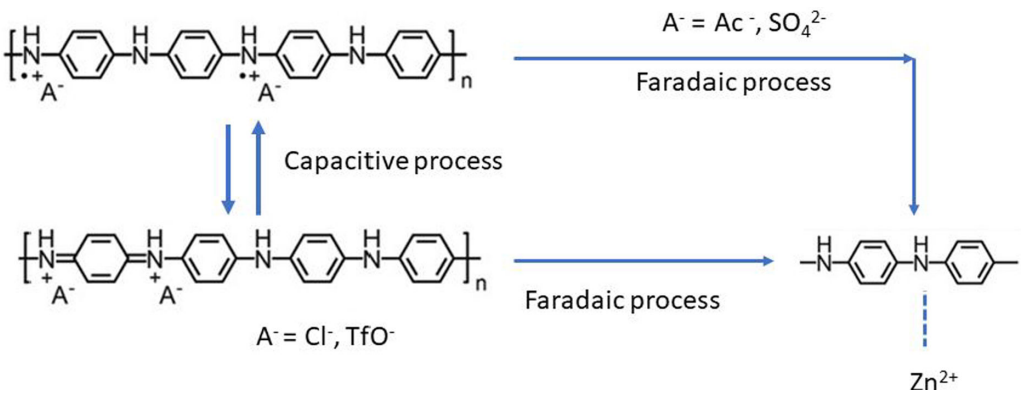

Scheme 1. Proposed reduction processes using different DES electrolytes.

when cycled in a DES-based electrolyte, which might be one of the reasons for the decrease in capacity. Furthermore, from N1s spectra in electronic supplementary material, fig. S7b, it is evident that N–O is formed for ZnAc and $ZnSO_4$ at 403.2 eV, whereas for $ZnCl_2$- and ZnTfO-based DES, features of amine and amide are observed. Therefore, the capacity loss for ZnAc and $ZnSO_4$ is higher compared to the other two electrolytes studied. Finally, the Zn morphology was also characterized to evaluate the possibility of dendrite formation. However, as can be seen in electronic supplementary material, fig. S8, no dendrite Zn formation was observed from the Zn salt containing DES-based electrolytes. However, for the $ZnCl_2$ electrolyte, non-uniform Zn structures are observed (electronic supplementary material, fig. S8a), which might have led to issues with long-term stability in the Zn battery.

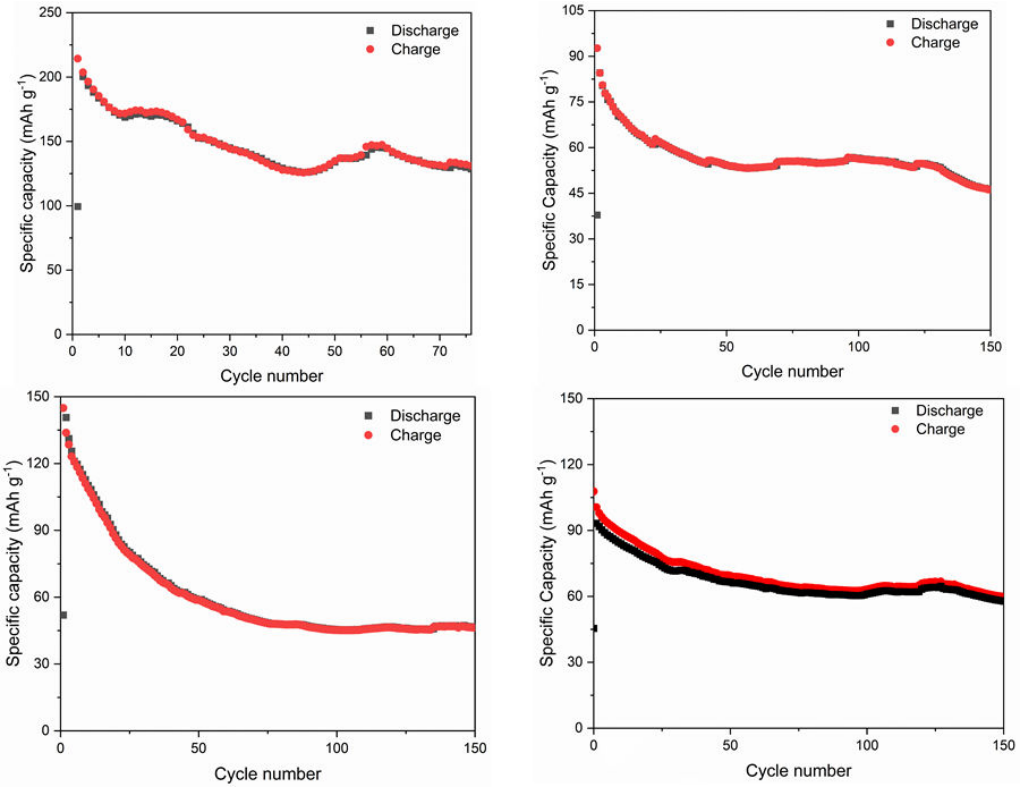

Figure 8. Zn–PANI battery performance at a current density of 0.5 A g^{-1} in the following electrolytes: (a) $ZnCl_2$: formamide + 40 wt% water, (b) $ZnSO_4$: formamide + 40 wt% water, (c) ZnAc: formamide + 40 wt% water and (d) ZnTf0: formamide + 40 wt% water.

4. Conclusion

In this paper, the influence of anions on a Zn–PANI battery in a DES electrolyte containing water is investigated. From spectroscopic analyses, it is evident that Zn solvation changes with the change in anion, which affects the Zn electrochemistry on PANI. From XPS and *in situ* Raman spectroscopic analyses, it was evident that for $ZnCl_2$- and ZnTfO-based DES, a capacitive process takes place, followed by Zn storage in PANI, whereas for ZnAc- and $ZnSO_4$-based DES, Zn is stored directly in the polymer matrix. The change in the storage mechanism leads to a change in the storage capacity in PANI. A rapid decrease in storage capacity was observed for ZnAc and $ZnSO_4$ electrolytes, whereas a gradual decrease in capacity was observed for $ZnCl_2$ and ZnTfO electrolytes. Among the different DES, the highest capacity was obtained for $ZnCl_2$-based DES electrolyte with an initial storage capacity of more than 200 mAh g^{-1}. However, capacity loss is a challenge for which new polymer composite cathodes need to be developed.

Data accessibility. Data have been made available in Brunel University London's repository via the Brunel Figshare database.

Supplementary material is available online [43].

Declaration of AI use. We have not used AI-assisted technologies in creating this article.

Authors' contributions. EÜ.: investigation, methodology, validation, writing—original draft; K.M.: investigation, methodology, writing—original draft; P.H.: data curation, formal analysis, investigation, methodology; Y.H.: supervision, writing—review and editing; S.G.: data curation, investigation, methodology, writing—review and editing; A.L.: conceptualization, funding acquisition, supervision, writing—review and editing.

All authors gave final approval for publication and agreed to be held accountable for the work performed therein.

Conflict of interest declaration. We declare we have no competing interests.

Funding. This research was wholly funded by EPSRC, EP/W015129/1. A CC BY or equivalent licence is applied to the author accepted manuscript arising from this submission, in accordance with the grant's open access conditions'. The X-ray photoelectron spectroscopy (XPS) data collection was performed at the EPSRC National Facility for XPS ('HarwellXPS', EP/Y023587/1, EP/Y023609/1, EP/Y023536/1, EP/Y023552/1 and EP/Y023544/1). Emine Kapancik Ülker thanks the Scientific and Technological Research Council of Türkiye (TUBITAK) for the support (Project No: 1059B192301430). The authors also thank Dr Sophia Hagani for SEM data.

References

1. Yin J, Zhang W, Alhebshi NA, Salah N, Alshareef HN. 2021 Electrochemical zinc ion capacitors: fundamentals, materials, and systems. *Adv. Energy Mater.* **11**, 00201. (doi:10.1002/aenm.202100201)
2. Shao Y, Shen F, Shao Y. 2021 Recent advances in aqueous zinc - ion hybrid capacitors: a minireview. *ChemElectroChem* **8**, 484–491. (doi:10.1002/celc.202001322)
3. Tang H, Yao J, Zhu Y. 2021 Recent developments and future prospects for zinc - ion hybrid capacitors: a review. *Adv. Energy Mater.* **11**, 2003994. (doi:10.1002/aenm.202003994)
4. Kang L, Cui M, Zhang Z, Jiang F. 2020 Rechargeable aqueous zinc - ion batteries with mild electrolytes: a comprehensive review. *Batter. Supercaps* **3**, 966–1005. (doi:10.1002/batt.202000060)
5. Li C, Wang L, Zhang J, Zhang D, Du J, Yao Y, Hong G. 2022 Roadmap on the protective strategies of zinc anodes in aqueous electrolyte. *Energy Storage Mater.* **44**, 104–135. (doi:10.1016/j.ensm.2021.10.020)
6. Mallick S, Raj CR. 2021 Aqueous rechargeable Zn-ion batteries: strategies for improving the energy storage performance. *ChemSusChem* **14**, 1987–2022. (doi:10.1002/cssc.202100299)
7. Verma V, Kumar S, Manalastas W, Jr Satish R, Srinivasan M. 2019 Progress in rechargeable aqueous Zinc - and aluminum - ion battery electrodes: challenges and outlook. *Adv. Sustain. Syst.* **3**, 1800111. (doi:10.1002/adsu.201800111)
8. Sui D, Wu M, Shi K, Li C, Lang J, Yang Y, Zhang X, Yan X, Chen Y. 2021 Recent progress of cathode materials for aqueous zinc-ion capacitors: carbon-based materials and beyond. *Carbon* **185**, 126–151. (doi:10.1016/j.carbon.2021.08.084)
9. Naskar P, Kundu D, Maiti A, Chakraborty P, Biswas B, Banerjee A. 2021 Frontiers in hybrid ion capacitors: a review on advanced materials and emerging devices. *ChemElectroChem* **8**, 1393–1429. (doi:10.1002/celc.202100029)
10. Wang H, Ye W, Yang Y, Zhong Y, Hu Y. 2021 Zn-ion hybrid supercapacitors: achievements, challenges and future perspectives. *Nano Energy* **85**, 105942. (doi:10.1016/j.nanoen.2021.105942)
11. Huang J, Qiu X, Wang N, Wang Y. 2021 Aqueous rechargeable zinc batteries: challenges and opportunities. *Curr. Opin. Electrochem.* **30**, 100801. (doi:10.1016/j.coelec.2021.100801)
12. Ma L, Li Q, Ying Y, Ma F, Chen S, Li Y, Huang H, Zhi C. 2021 Toward practical high-areal-capacity aqueous zinc-metal batteries: quantifying hydrogen evolution and a solid-ion conductor for stable zinc anodes. *Adv. Mater.* **33**, e2007406. (doi:10.1002/adma.202007406)
13. Shang Y, Kundu D. 2022 Understanding and performance of the zinc anode cycling in aqueous zinc - ion batteries and a roadmap for the future. *Batter. Supercaps* **5**, e202100394. (doi:10.1002/batt.202100394)
14. Xie C, Li Y, Wang Q, Sun D, Tang Y, Wang H. 2020 Issues and solutions toward zinc anode in aqueous zinc - ion batteries: a mini review. *Carbon Energy* **2**, 540–560. (doi:10.1002/cey2.67)
15. Han C, Li W, Liu HK, Dou S, Wang J. 2020 Principals and strategies for constructing a highly reversible zinc metal anode in aqueous batteries. *Nano Energy* **74**, 104880. (doi:10.1016/j.nanoen.2020.104880)
16. Geng Y *et al*. 2022 Electrolyte additive engineering for aqueous Zn ion batteries. *Energy Storage Materials* **51**, 733–755. (doi:10.1016/j.ensm.2022.07.017)

17. Wu S, Chen Y, Jiao T, Zhou J, Cheng J, Liu B, Yang S, Zhang K, Zhang W. 2019 An aqueous zn - ion hybrid supercapacitor with high energy density and ultrastability up to 80 000 cycles. *Adv. Energy Mater.* **9**, 02915. (doi:10.1002/aenm.201902915)
18. Zhang L, Liu Z, Wang G, Feng J, Ma Q. 2021 Developing high voltage Zn(TFSI)2/Pyr14 TFSI/AN hybrid electrolyte for a carbon-based Zn-ion hybrid capacitor. *Nanoscale* **13**, 17068–17076. (doi:10.1039/D1NR03879F)
19. MacFarlane DR *et al*. 2016 Ionic liquids and their solid-state analogues as materials for energy generation and storage. *Nat. Rev. Mater.* **1**, 15005. (doi:10.1038/natrevmats.2015.5)
20. Zheng Y, Wang D, Kaushik S, Zhang S, Wada T, Hwang J, Matsumoto K, Hagiwara R. 2022 Ionic liquid electrolytes for next-generation electrochemical energy devices. *EnergyChem* **4**, 100075. (doi:10.1016/j.enchem.2022.100075)
21. Qiu H *et al*. 2019 Zinc anode-compatible in-situ solid electrolyte interphase via cation solvation modulation. *Nat. Commun.* **10**, 5374. (doi:10.1038/s41467-019-13436-3)
22. Wu J, Liang Q, Yu X, Lü Q, Ma L, Qin X, Chen G, Li B. 2021 Deep eutectic solvents for boosting electrochemical energy storage and conversion: a review and perspective. *Adv. Funct. Mater.* **31**, 2011102. (doi:10.1002/adfm.202011102)
23. Liu Z, Pulletikurthi G, Lahiri A, Cui T, Endres F. 2016 Suppressing the dendritic growth of zinc in an ionic liquid containing cationic and anionic zinc complexes for battery applications. *Dalton Trans.* **45**, 8089–8098. (doi:10.1039/C6DT00969G)
24. Cui T, Lahiri A, Carstens T, Borisenko N, Pulletikurthi G, Kuhl C, Endres F. 2016 Influence of water on the electrified ionic liquid/solid interface: a direct observation of the transition from a multilayered structure to a double-layer structure. *J. Phys. Chem. C* **120**, 9341–9349. (doi:10.1021/acs.jpcc.6b02549)
25. Lu X, Tao L, Qu K, Zhang Y, Liu C, Godin R, Liu J. 2022 A low-concentration eutectic electrolyte for superior cycling ability of aqueous zinc-ion capacitors. *J. Mater. Chem. A.* **10**, 20273–20282. (doi:10.1039/D2TA05573B)
26. Zhao J *et al*. 2019 'Water-in-deep eutectic solvent' electrolytes enable zinc metal anodes for rechargeable aqueous batteries. *Nano Energy* **57**, 625–634. (doi:10.1016/j.nanoen.2018.12.086)
27. Lahiri A, Hirani P, Haghani S, Endres F. 2024 Effect of water on Zn electrodeposition from a deep eutectic solvent. *J. Electrochem. Soc.* **171**, 012505. (doi:10.1149/1945-7111/ad1d99)
28. Pereira LM, Alves WA. 2011 Solute–solvent interactions in formamide and zinc chloride solutions: an investigation by raman spectroscopy. *Vib. Spectrosc.* **56**, 250–254. (doi:10.1016/j.vibspec.2011.03.005)
29. Lin X, Wang Z, Ge L, Xu J, Ma W, Ren M, Liu W, Yao J, Zhang C. 2022 Electrolyte modification for long - life zn ion batteries: achieved by methanol additive. *ChemElectroChem* **9**, e202101724. (doi:10.1002/celc.202101724)
30. Fleischmann S, Mitchell JB, Wang R, Zhan C, Jiang D en, Presser V, Augustyn V. 2020 Pseudocapacitance: from fundamental understanding to high power energy storage materials. *Chem. Rev.* **120**, 6738–6782. (doi:10.1021/acs.chemrev.0c00170)
31. Chen GZ. 2021 Linear and non-linear pseudocapacitances with or without diffusion control. *Prog. Nat. Sci. Mater. Int* **31**, 792–800. (doi:10.1016/j.pnsc.2021.10.011)
32. Ziaeimoghaddam F, Arefinia R. 2022 Investigation of the effect of doping/dedoping on the redox behavior of polyaniline film: experimental and modeling approach. *Progress in Organic Coatings* **170**, 106952. (doi:10.1016/j.porgcoat.2022.106952)
33. Liao X, Pan C, Yan H, Zhu Y, Pan Y, Yin C. 2022 Polyaniline-functionalized graphene composite cathode with enhanced Zn2+ storage performance for aqueous zinc-ion battery. *Chem. Eng. J.* **440**, 135930. (doi:10.1016/j.cej.2022.135930)
34. Gong J *et al*. 2022 Zinc-ion storage mechanism of polyaniline for rechargeable aqueous zinc-ion batteries. *Nanomaterials* **12**, 1438. (doi:10.3390/nano12091438)
35. Kang ET, Neoh KG, Khor SH, Tan KL, Tan BTG. 1990 X.p.s. studies of charge transfer interactions in some polyaniline complexes. *Polymer* **31**, 202–207. (doi:10.1016/0032-3861(90)90106-9)
36. Golczak S, Kanciurzewska A, Fahlman M, Langer K, Langer J. 2008 Comparative XPS surface study of polyaniline thin films. *Solid State Ion.* **179**, 2234–2239. (doi:10.1016/j.ssi.2008.08.004)

37. Chen Y, Kang ET, Neoh KG, Lim SL, Ma ZH, Tan KL. 2001 Intrinsic redox states of polyaniline studied by high-resolution X-ray photoelectron spectroscopy. *Colloid Polym. Sci.* **279**, 73–76. (doi:10.1007/s003960000418)
38. Mahat MM, Mawad D, Nelson GW, Fearn S, Palgrave RG, Payne DJ, Stevens MM. 2015 Elucidating the deprotonation of polyaniline films by X-ray photoelectron spectroscopy. *J. Mater. Chem. C.* **3**, 7180–7186. (doi:10.1039/C5TC01038A)
39. Trchová M, Morávková Z, Bláha M, Stejskal J. 2014 Raman spectroscopy of polyaniline and oligoaniline thin films. *Electrochimica Acta* **122**, 28–38. (doi:10.1016/j.electacta.2013.10.133)
40. Bláha M, Bouša M, Valeš V, Frank O, Kalbáč M. 2021 Two-dimensional CVD-graphene/polyaniline supercapacitors: synthesis strategy and electrochemical operation. *ACS Appl. Mater. Interfaces* **13**, 34686–34695. (doi:10.1021/acsami.1c05054)
41. Mansour AE *et al*. 2022 Understanding the evolution of the Raman spectra of molecularly p-doped poly(3-hexylthiophene-2,5-diyl): signatures of polarons and bipolarons. *Phys. Chem. Chem. Phys.* **24**, 3109–3118. (doi:10.1039/d1cp04985b)
42. Vujković MJ, Etinski M, Vasić B, Kuzmanović B, Bajuk-Bogdanović D, Dominko R, Mentus S. 2021 Polyaniline as a charge storage material in an aqueous aluminum-based electrolyte: can aluminum ions play the role of protons? *J. Power Sources* **482**, 228937. (doi:10.1016/j.jpowsour.2020.228937)
43. Ülker E, Mohammadzadeh K, Hirani P, He Y, Guan S, Lahiri A. 2026 Supplementary material from: Mechanism of Zn storage in polyaniline in deep eutectic solvent-water mixtures: effect of anion and interfacial phenomena. Figshare. (doi:10.6084/m9.figshare.c.8369279)